

Large eddy simulation of marine flows over complex geometries using a massively parallel unstructured overset method

T. Kroll, N. Morse, W. Horne and K. Mahesh

(Department of Aerospace Engineering & Mechanics, University of Minnesota, USA)

ABSTRACT

A novel unstructured overset method developed by Horne and Mahesh (2019a,b) is used to perform large-eddy simulation (LES) of marine flows over complex geometries. Wall-resolved overset LES on an idealized submarine geometry (DARPA SUBOFF) shows good agreement with available experimental data. For the marine propeller David Taylor Model Basin (DTMB) 4381 in forward mode and crashback, mean flow fields and propeller load statistics show good agreement with experiments and previous simulations. These cases are used as building-blocks towards the goal of simulating maneuvering, self-propelled marine vessels.

INTRODUCTION

Flows over marine bodies are characterized by high Reynolds numbers and complex geometries, which pose major challenges to their study both experimentally and computationally. Marine vehicles can typically be described by a long, slender hull, a set of appendages acting as control surfaces, and a propeller, most often mounted at the stern. Figure 1 shows an example of such a hull-form in a water tunnel. In the case of a maneuvering, self-propelled vehicle, the performance of the propeller depends on its inflow, which consists of the complex boundary layer incoming from the hull. At the stern, the hull boundary layer is turbulent and is affected by pressure gradients and the hull curvature, potentially leading to separation. Additional complications to the propeller inflow originate from the junction vortices produced by the boundary layer interactions with the appendages. During a quick, decelerating maneuver, the propeller goes into an off-design mode known as crashback where the propeller rotation is reversed as the vehicle is still moving forward to create negative thrust. The turbulent hull boundary layer interacts with the propeller-induced reverse flow, forming a highly unsteady ring vortex, the prominent flow feature associated with this condition. The propeller blades experience large flow separation,

creating highly unsteady loads with low frequencies and high amplitudes. These loads not only affect the blade structure, but also the vessel's maneuverability because of the significant moments produced by the propeller about the center of gravity of the vehicle.

In order to successfully simulate a maneuvering marine vehicle, one needs to address the challenges presented by the essential aspects of the flow. The evolution of the turbulent hull boundary layer and appendage wakes requires high wall resolution, and thus large meshes with high computational cost. The hull boundary layer's interaction with the propeller-induced flow, especially for a maneuver like crashback, presents the challenge of long run times needed to capture low frequency loads essential to maneuverability. The complex geometry of the hull and propeller blades makes quality grid generation a challenge. Finally, the computations must represent the relative movements between the hull, propeller, and control surfaces, as well as maneuvering motions.

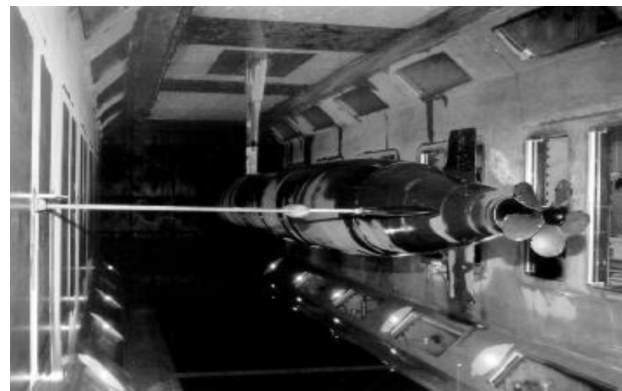


Figure 1: Appended hull with attached propeller P4381 in a water tunnel (Bridges, 2004).

In the advent of increased computational power, the capability of computational fluid dynamics (CFD) to simulate bigger and more complex problems has grown.

Direct numerical simulation (DNS) of complex bodies at the high Reynolds numbers associated with marine flows is not computationally feasible due to resolution requirements (Moin and Mahesh, 1998). Yang and Löhrner (2003) and Kim et al. (2013) have shown the capability of Reynolds-averaged Navier-Stokes (RANS) for these types of flows. However, RANS has been shown to fail in correctly predicting crashback flows (Davoudzadeh et al., 1997; Chen and Stern, 1999). Large-eddy simulation (LES) is a method in which the large scales of motion are resolved, while the effect of the small scales is modelled. As numerical algorithms and computational capabilities have improved, LES has been shown to be a good middle ground between RANS and DNS for complex marine flow applications (Mahesh et al., 2015). Bensow et al. (2006) and Alin et al. (2010) reviewed the capability of RANS, detached-eddy simulation (DES) and LES to simulate flow over an idealized hull geometry (DARPA SUBOFF) and showed that LES represented the unsteady flow field features the best but with greater computational cost. LES has also been successful in simulating a variety of complex marine flows (Verma et al., 2012; Kumar and Mahesh, 2017; Jang and Mahesh, 2013). Thus, LES is the selected approach in this study. To address the ability of the numerical method to handle general, relative movement between bodies, as required for maneuvering calculations, the method used in the present computations is an unstructured overset grid method with the capability of solving arbitrary overlapping and moving meshes (Horne and Mahesh, 2019a,b). It uses the Arbitrary Lagrangian-Eulerian (ALE) formulation of the incompressible Navier-Stokes equations where the motion of the body or grid is incorporated into the equations.

Due to the overall complexity of simulating a maneuvering marine vehicle, the present study splits the problem into several independent building-block problems. These cases are validated separately to address their specific challenges. The present work considers independently flow over a notional submarine hull, the DARPA SUBOFF (Groves et al., 1989), as well as the marine propeller P4381, both of which have been studied extensively in past experiments and computations.

The DARPA SUBOFF is a generic hull geometry consisting of an axisymmetric hull with a fairwater (sail) near the front of the hull and four appendages near the stern (Groves et al., 1989). Two configurations of this hull geometry are considered in the present study: the axisymmetric bare hull configuration without appendages (AFF1) and the fully appended hull (AFF8), as shown in Figure 2. Flow over the bare hull has been studied experimentally by Huang et al. (1992) at $Re = 1.2 \times 10^7$ and by Jiménez et al. (2010a), who studied the wake over a Reynolds number range $1.1 \times 10^6 - 6.7 \times 10^7$.

Kumar and Mahesh (2018b) performed wall-resolved LES over the bare hull at $Re = 1.1 \times 10^6$, showing good agreement with the above experiments and commenting on the axisymmetric turbulent boundary layer and the wake development. Jiménez et al. (2010b) experimentally studied the effect of appendages on the wake of the fully appended SUBOFF over a Reynolds number range $4.9 \times 10^5 - 1.8 \times 10^6$. Wall-resolved LES of this geometry at $Re = 1.2 \times 10^6$ was performed by Posa and Balaras (2016) using an immersed boundary method, with good agreement with experiments. They later expanded upon this work by attaching an INSEAN E1619 propeller to the hull to study the flow over the hull in a self-propulsion configuration at the same Reynolds number (Posa and Balaras, 2018). Recently, Posa and Balaras (2020) performed LES over the same appended geometry at $Re = 1.2 \times 10^7$, comparing with their previous study at lower Re to investigate the Reynolds number effects on the flow over the hull. Chase et al. (2013) used delayed detached eddy simulation (DDES) with an overset method to simulate the appended SUBOFF geometry and E1619 propeller in towed, self-propelled, and maneuvering conditions.

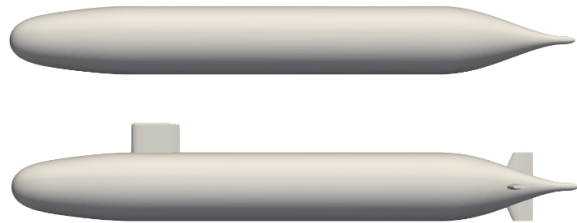


Figure 2: Geometry of axisymmetric bare hull (AFF1) and fully appended (AFF8) DARPA SUBOFF (Groves et al., 1989).

Marine propeller P4381 is a five-bladed, right-handed propeller with variable pitch, and no skew or rake. It has been studied both experimentally and through simulations. Jiang et al. (1997) used Particle Image Velocimetry (PIV) to study the structure of the unsteady ring vortex and its relationship to the unsteady loads in crashback. Jessup et al. (2004, 2006) performed experiments on open and ducted propeller configurations at different operating conditions with detailed measurements of flow field using PIV and Laser Doppler Velocimetry (LDV) as well as measurements of the propeller unsteady loads. At design conditions, complex flow structures like the axial hub vortex and helical tip vortices are convected downstream of the rotor. Kumar and Mahesh (2017) performed LES of the same geometry at Reynolds number $Re = 894,000$ and looked

at the complex wake interactions and propeller loads. Vyšohlid and Mahesh (2006), Chang et al. (2008), and Jang and Mahesh (2013) used LES to study the details and origins of the unsteady loads in crashback as well as the flow field at numerous advance ratios J at $Re = 480,000$.

In this study, we will examine in detail the building-block problems representative of the essential parts to successfully simulate a fully maneuvering body using LES. A novel unstructured overset grid method is applied and its validation is evaluated and discussed. For the bare hull and appended hull, flow fields are examined, with comparisons to experimental measurements of pressure and skin friction coefficients. For the P4381 marine propeller in both forward mode of operation and crashback, we will examine the propeller loads and the flow field around the propeller and in the near wake.

SIMULATION DETAILS

Numerical Method

The incompressible Navier-Stokes equations with an Arbitrary Lagrangian-Eulerian (ALE) formulation are used. The mesh velocity is included in the convection term which avoids tracking multiple reference frames for arbitrary motion of meshes. For LES, large scales are directly accounted for by the spatially filtered Navier-Stokes equations, and small scales are modeled. The filtered Navier-Stokes equations with the ALE formulation are as follows:

$$\begin{aligned} \frac{\partial \bar{u}_i}{\partial t} + \frac{\partial}{\partial x_j} (\bar{u}_i \bar{u}_j - \bar{u}_i V_j) &= -\frac{\partial \bar{p}}{\partial x_i} + \nu \frac{\partial^2 \bar{u}_i}{\partial x_j \partial x_j} - \frac{\partial \tau_{ij}}{\partial x_j}, \\ \frac{\partial \bar{u}_i}{\partial x_i} &= 0, \end{aligned} \quad (1)$$

where u_i is the velocity in the inertial frame, p is the pressure, ν is the kinematic viscosity, V_j is the grid velocity, the overbar $(\bar{\cdot})$ denotes the spatial filter and $\tau_{ij} = \bar{u}_i \bar{u}_j - \bar{u}_i \bar{u}_j$ is the sub-grid stress tensor. To model the sub-grid stress terms, the dynamic Smagorinsky model proposed by Germano et al. (1991) and modified by Lilly (1992) is used. In addition, the Lagrangian time scale is dynamically computed based on surrogate-correlation of the Germano-identity error (Park and Mahesh, 2009). This approach has shown good performance for a variety of flows including a marine propeller in crashback (Verma and Mahesh, 2012).

When addressing the computational challenges of high Reynolds numbers and complex geometries, it is critical that the numerical method does not introduce additional numerical dissipation that would artificially damp the smallest resolved scales. Mahesh et al. (2004) developed an unstructured numerical algorithm for LES of complex flows that emphasizes discrete kinetic energy

conservation, ensuring robustness at high Reynolds number without numerical dissipation. This method has been successful in simulating a variety of complex marine flows (Verma et al., 2012; Kumar and Mahesh, 2017; Jang and Mahesh, 2013; Kumar and Mahesh, 2018b). In order to address rotational motion, these previous simulations were performed with the incompressible Navier-Stokes equations being solved in a reference frame that rotates with the propulsor. To address the ability of the numerical method to handle general, relative movement between bodies, the method used in the present computations is an unstructured overset grid method based on the above algorithm of Mahesh et al. (2004) with the capability of solving arbitrary overlapping and moving meshes (see Horne and Mahesh, 2019a,b). It uses an ALE method coupled to a 6 degrees of freedom rigid body equation system (6-DOF) for body motion. At boundary edges of meshes, boundary conditions are obtained by performing flow field reconstructions using overlapping meshes and geometry. This enables the use of body-fitted meshes, ensuring high resolution on the relevant geometries while aiding to save on overall mesh size and increased grid generation flexibility. In addition, this method addresses the conservation challenges of overset methods through use of a volume-conservative supercell interpolation. To address additional computational cost and scaling challenges of overset methods, it uses a novel communication strategy, scaling to $O(10^5)$ meshes and processors. The algorithm has been validated for a variety of problems over a range of Reynolds numbers.

Geometry and Computational Mesh

The geometries used in this study focus on building-block sections for a fully appended maneuvering body. This includes the bare hull, appendages and the propulsor. For the propulsor, CAD for P4381 is utilized to represent the geometry in grid generation software. Care is taken in the mesh generation process as it is important to ensure good quality grid when using a non-dissipative scheme at high Reynolds numbers.

When setting up the overset cases, there are several important factors to consider in order to ensure an accurate, robust solution. Due to the use of arbitrary overlapping meshes, it is important that there is enough overlap between meshes. This is important to make sure that the interpolation boundary control volumes find interpolation partner pairs. Though the supercell reconstruction helps give more flexibility, care is taken to avoid large resolution differences at interpolation boundaries, avoiding control volume ratios greater than 2 to 1 in each independent direction.

Bare Hull and Appended Hull DARPA SUBOFF

Simulations are performed for flow over the unappended axisymmetric SUBOFF at $Re = 1.1 \times 10^6$ and for the fully appended SUBOFF at $Re = 1.2 \times 10^6$ based on the hull length and free-stream velocity. Figure 3 shows the cylindrical computational domain used for both cases, which was modelled after the computational domain of Kumar and Mahesh (2018b). The domain has length $28.8D_H$ and radius $6D_H$, where D_H is the diameter of the mid-section of the hull, and extends from $3D_H$ upstream of the front of the hull to $17.2D_H$ downstream of the stern of the hull.

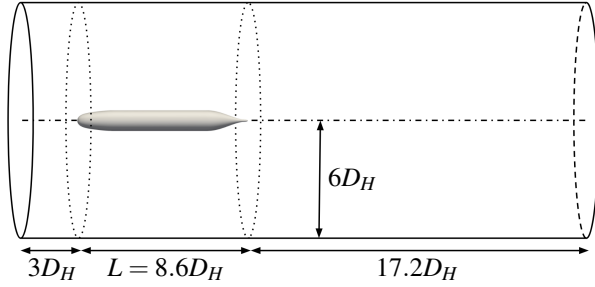


Figure 3: Computational domain for simulations of the DARPA SUBOFF.

For the bare hull case, the computational domain is split into three stationary overset grids. These are a body-fitted grid attached to the hull, a cylindrical grid located downstream of the hull for refinement of the wake, and a cylindrical background mesh on which the boundary conditions are imposed. Free-stream boundary conditions are imposed at the inflow and radial boundaries and a convective boundary condition is imposed at the outflow boundary. The computational grid for the hull must be refined in the near-wall region to capture the thin boundary layer and near-wall streaks, which contribute to the skin friction at the wall and the viscous drag of the hull. To capture these streaks, the hull grid is refined with 1600 cells in the azimuthal direction, corresponding to an azimuthal resolution of $a^+ \Delta \theta = 11$, where $a = D_H/2$ is the local radius of curvature at the mid-section of the hull and $a^+ = au_\tau/\nu$. In the boundary layer, the first wall-normal spacing is specified as $0.0003D_H$ with a growth rate of 1.01 away from the hull, producing a nominal first wall-normal spacing $y^+ = 1$ and a nominal streamwise spacing of $x^+ \leq 33$. As in the experiments of Jiménez et al. (2010a), the boundary layer is tripped at $x/D_H = 0.75$. This is implemented numerically by applying a steady wall-normal velocity of $0.05U_\infty$ at this x -location. The overall grid for the bare hull computation consists 712 million hexahedral control volumes partitioned over 9504 processors.

In the case of the appended hull, additional stationary overset grids for the sail and the four stern appendages are added, bringing the total control volume count to 827 million cells partitioned over 11,396 processors. The meshing of the complex appended hull geometry is simplified by meshing the sail and stern appendages separately from the hull. With this strategy, the complexity of each mesh is reduced and focus is shifted to matching grid resolutions between the overset meshes. Iterations of the appendage meshes can be performed while the other meshes are left unchanged, lowering the meshing time and overall computational cost. The boundary layer tripping location is changed to $x/D_H = 0.25$ for the appended hull, consistent with the experiments of Jiménez et al. (2010b). The required wall-normal trip velocity is $0.08U_\infty$ at this location in order to fully trip the boundary layer. The difference in trip velocity magnitude compared to the bare hull case is due to the location of the trip in a favorable pressure gradient. The details of the overset grids for the hull computations are given in table 1.

Grid	CVs	Procs
Background	113M	1540
Hull	429M	5676
Wake	170M	2288
Sail	91M	1188
Stern appendages	$6M \times 4$	176×4

Table 1: Details for the SUBOFF overset grids including number of control volumes and number of processors.

Forward Mode and Crashback for Propeller P4381

Simulations are performed for the marine propeller P4381, details of the geometry are given in (Jessup et al., 2004, 2006). The advance ratio J and the Reynolds number based on the propeller diameter, Re are defined below:

$$J = \frac{U}{nD_P}, \quad Re = \frac{UD_P}{\nu} \quad (2)$$

where U is the free-stream velocity, $D_P = 12.0$ in is the propeller disk diameter, n is the rotational speed and ν is the kinematic viscosity. Thrust T is defined as the axial component of the force. The axial component of the moment of the force is the torque Q . F_H and F_V are the horizontal and vertical components of the force whose vector sum yields the total side force F_T . ρ is the fluid density. Non-dimensional thrust K_T , torque coefficient K_Q and side-force coefficient K_S are defined as:

$$K_T = \frac{T}{\rho n^2 D_P^4}, K_Q = \frac{Q}{\rho n^2 D_P^5}, K_S = \frac{\sqrt{F_H^2 + F_V^2}}{\rho n^2 D_P^4} \quad (3)$$

$\langle K_T \rangle$ represents the mean of the coefficient K_T and $\sigma(K_T)$ the standard deviation.

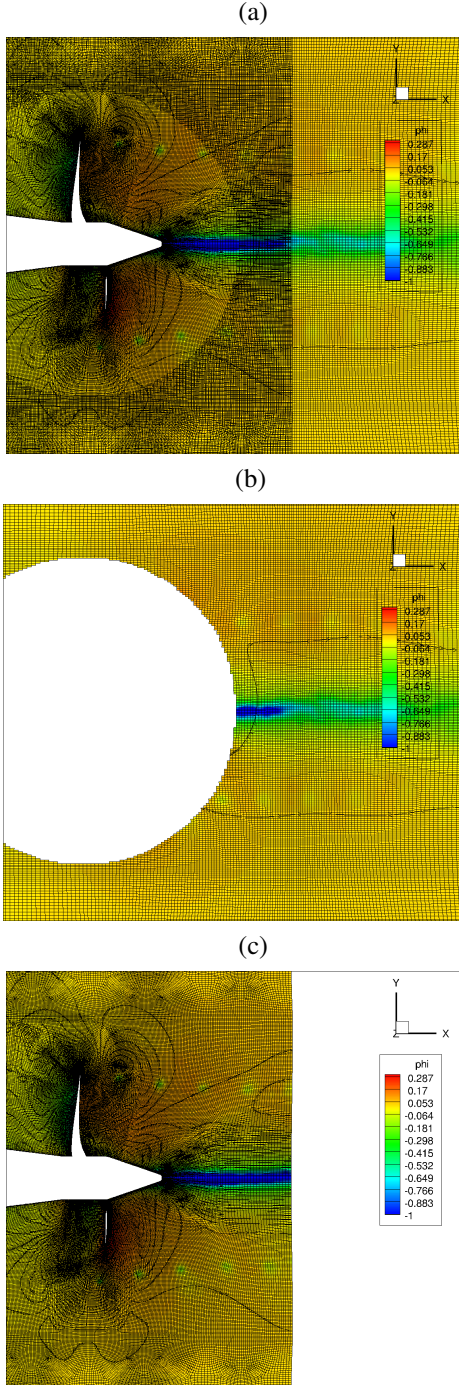


Figure 4: a) The two grids together, b) The background grid and c) the propeller grid. A spherical cut is used to remove redundant control volumes in the near propeller region.

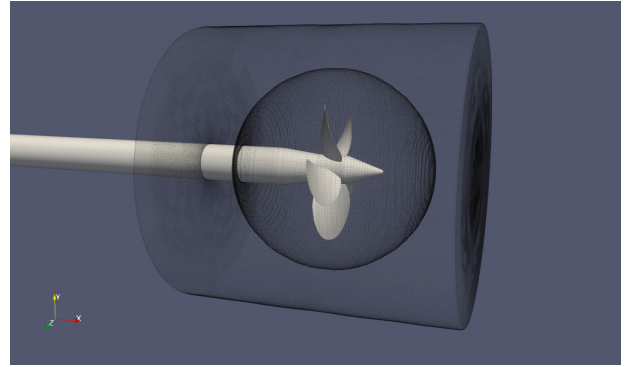


Figure 5: The mesh configuration for the forward mode case. A spherical projected cut was used to remove redundant control volumes near the propeller on the background mesh. The cylindrical outer edge of the propeller mesh is also shown. The control volumes on these edges obtain boundary conditions by performing flow field reconstructions using overlapping control volumes from the other mesh.

Two modes of operation are validated in this study. For forward mode or design condition, the case is set up at a Reynolds number $Re = 894,000$ and the propeller rotates at an advance ratio $J = 0.889$. The mesh is fully hexahedral in order to capture well the helical tip vortices as they convect downstream. This mesh is similar to (Kumar and Mahesh, 2017) but with lower resolution in both the near propeller region and far wake. It also has a longer region upstream of propeller, to make grid generation for both cases easier by utilizing the same domain. On the blade, the first layer has a minimum wall-normal spacing of $0.0017 D_P$ and a growth ratio of 1.02. On other surfaces, the resolution is $0.0125 D_P$. The computational domain is a cylinder of diameter $7.0D_P$ and length $14.0D_P$ as shown on figure 6. There are two meshes in the simulation. First, a cylindrical shaped background mesh that is stationary. The inflow, outflow (convective) and far field boundary conditions are set on this mesh. This mesh contains just the hub and no propeller. Redundant control volumes are dynamically removed using a spherical projection from the center of the propeller, see figures (4, 5). The second mesh is the cylindrical propeller mesh which includes the 5 propeller blades is rotated at the rotational velocity ω to match the advance ratio J using the equation below:

$$\omega = 2\pi n \quad (4)$$

$\omega \times R$ boundary conditions the are set on the blade mesh surfaces and the hub surface contained in the propeller mesh. More information on the size and partitioning of the meshes is presented on table 2. The mesh

configuration and interpolation edges of these two meshes can be seen on figure 4.

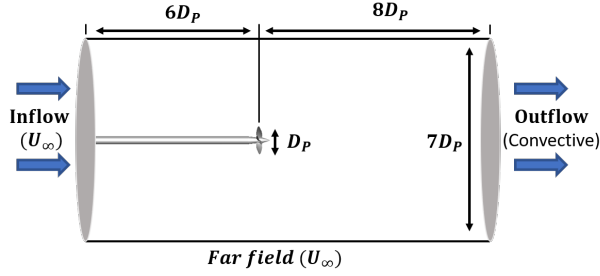


Figure 6: Computational domain and the boundary conditions on the boundaries

<i>Grid</i>	<i>CVs</i>	<i>Procs</i>
Background	13.5M	436
Propeller	23.0M	716
Total	36.5M	1152

Table 2: Details for the grids in forward mode, including the number of control volumes and the number of processors.

For crashback, the propeller rotates at an advance ratio of $J = -0.7$ and Reynolds number $Re = 480,000$. The domain and outer edges of the background grid are the same as those used in forward mode case. To utilize the flexibility of the method in reducing computational cost and to use the grid generation flexibility, the background mesh is generated with a cylindrical cut in the hub cap region, see figure 7. A manual cut is used to remove redundant control volumes during grid generation compared to the dynamic cutting in the forward mode case. The propeller mesh, is similar to the coarse mesh in (Jang and Mahesh, 2013) where a pill-box of 2.8 million tetrahedral cells is used in the near blade area. On the blade surface, four prism layers are extruded at a height of $0.0017D_P$ and a growth ratio of 1.01. On other surfaces the resolution is the same as on the blades. Because of the separated nature of this flow, resolving the attached boundary layer is not needed to make accurate predictions. More information on the meshes is presented on table 3.

<i>Grid</i>	<i>CVs</i>	<i>Procs</i>
Background	5.2M	336
Propeller	3.7M	240
Total	8.7M	576

Table 3: Details for the grids in crashback, including the number of control volumes and the number of processors.

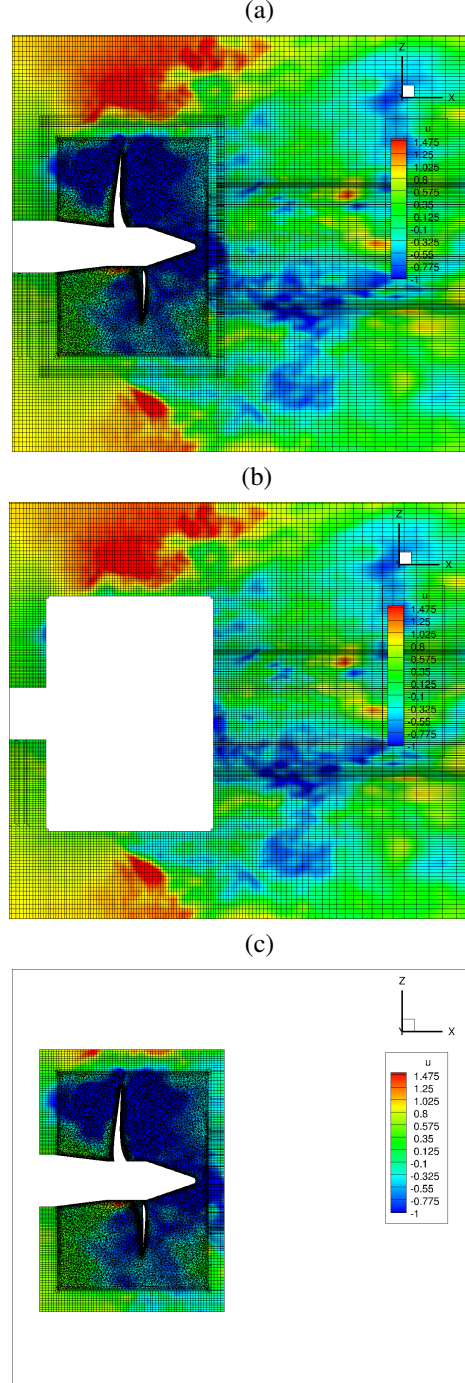


Figure 7: a) The two grids together, b) The background grid and c) the propeller grid. A manual, cylindrical cut is used to remove redundant control volumes during grid generation. Note that important flow structures like the ring vortex are communicated at the interpolation edges between the two meshes.

RESULTS

Bare Hull DARPA SUBOFF

Simulation of the bare hull SUBOFF is performed at $Re = 1.1 \times 10^6$, based on the hull length, using wall-resolved LES using a timestep of $tU/D_H = 0.0012$. The simulation was run at the target Reynolds number for approximately 2 flow-through times to discard transients and another 1.5 flow-throughs to collect statistics, equating to nearly 1.4 million CPU hours. The instantaneous flow-field around the bare hull is shown in Figure 8, where the rapid thickening of the turbulent boundary layer over the adverse pressure gradient imposed by the tapering stern is visible, followed by the development of the wake. The accurate simulation of the hull boundary layer approaching the stern is critical for capturing the behavior of the stern boundary layer and the proper wake width. In the case of a propelled hull, the simulation of the stern boundary layer is also critical to produce the correct propeller inflow.

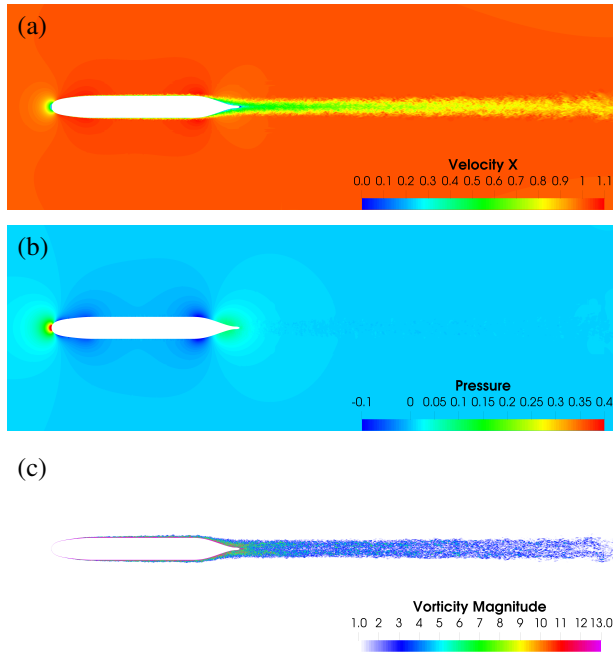


Figure 8: Flow over the bare hull: instantaneous (a) velocity, (b) pressure, and (c) vorticity magnitude in the (x,y) plane.

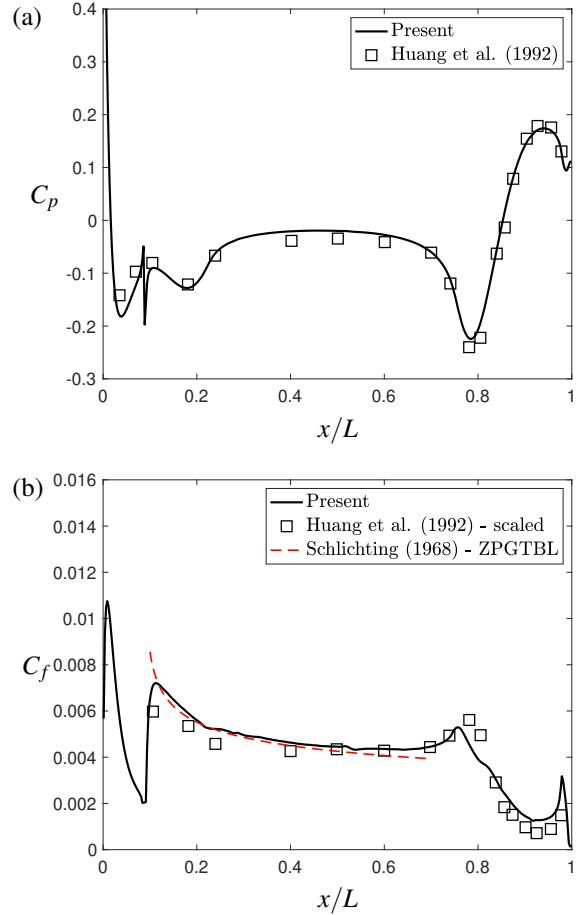


Figure 9: Flow over the bare hull: (a) C_p and (b) C_f on the hull. Experimental data at $Re = 1.2 \times 10^7$ (Huang et al., 1992) and the analytical C_f curve for a flat plate ZPGTBL (Schlichting, 1968) are shown for comparison. The experimental C_f is scaled to the Reynolds number of the present simulation using the scaling law $C_f \sim Re^{-0.2}$.

The pressure and skin-friction coefficients on the hull are compared to the experimental data of Huang et al. (1992) in Figure 9. The pressure and skin-friction coefficients are defined as

$$C_p = \frac{p - p_\infty}{0.5\rho U_\infty^2} \quad (5)$$

$$C_f = \frac{\tau_w}{0.5\rho U_\infty^2} \quad (6)$$

where p_∞ is the reference pressure and τ_w is the shear stress at the wall. Note that the experiments of Huang et al. (1992) were conducted at $Re = 1.2 \times 10^7$. Since C_p is fairly insensitive to Re for high Re , the experimental data is compared directly to the present results in Figure 9 (a). The agreement with the experiments is good over much of

the hull. Note that the spike in C_p on the bow corresponds to the trip location at $x/D_H = 0.75$. Following the bow, a long zero pressure gradient axisymmetric boundary layer develops along the mid-section of the hull. Over the stern, the hull tapers to form a convex surface at $x/L \approx 0.8$ and the flow accelerates with a corresponding drop in pressure and increase in skin-friction coefficient. Immediately following this acceleration, the boundary layer experiences a strong adverse pressure gradient, causing it to rapidly thicken and displacing the peak of turbulent kinetic energy away from the wall, as observed by Posa and Balaras (2016) and Jiménez et al. (2010a).

As mentioned above, the experiments were conducted at a higher Reynolds number than the present computations, so it is not possible to directly compare the present skin friction results with the experimental results. However, the skin-friction coefficient is known to scale with Re as $C_f \sim Re^{-0.2}$ for a high Re attached zero pressure gradient boundary layer. In Figure 9 (b), this scaling is applied to the experimental data of Huang et al. (1992) to scale the data to the present Re for comparison. Also shown in the figure is the analytical C_f curve of a flat plate zero pressure gradient turbulent boundary layer (ZPGTBL) given by Schlichting (1968) as

$$C_f = 0.0576 \left(\frac{U_\infty x}{\nu} \right)^{-\frac{1}{5}} \quad (7)$$

The agreement with the C_f slope from the above equation is good over the zero pressure gradient region of the hull away from the influence of the hull's longitudinal curvature. The above relation for a flat plate ZPGTBL is suitable for comparison with the present computations since the ratio of the boundary layer thickness to the local radius of curvature of the body is small in this region, so effects of transverse curvature are small. Kumar and Mahesh (2018a) obtained relations for C_f based on integral boundary layer quantities for axisymmetric boundary layers evolving under pressure gradients. They determined that C_f is always increased by the presence of transverse curvature as long as the Rotta-Clauser pressure-gradient parameter (Rotta, 1953; Clauser, 1954) is positive. As predicted, the effect of transverse curvature increases C_f above levels for a flat plate ZPGTBL as the boundary layer thickens over the hull as the ratio of the boundary layer thickness to the radius of curvature of the hull grows with x/L .

Figure 11 shows the mean streamwise velocity in the axisymmetric wake normalized by the velocity at the edge of the wake compared to the experimental data of Jiménez et al. (2010a) at the same Reynolds number.

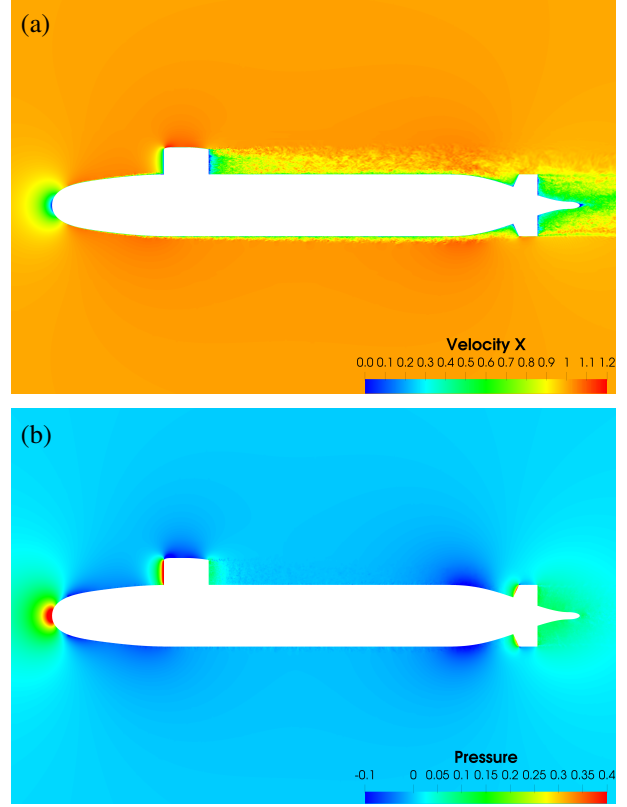


Figure 10: Flow over the appended hull: instantaneous (a) velocity and (b) pressure in the (x,y) plane.

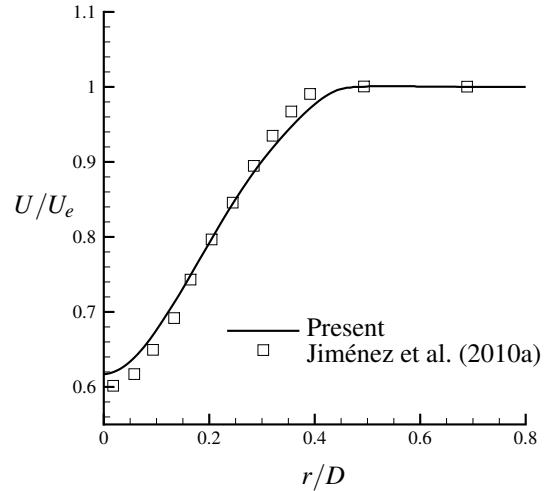


Figure 11: Flow over the bare hull: streamwise mean velocity normalized by the velocity at the edge of the axisymmetric wake at a distance $3D$ from the downstream end of the hull. Results are compared to measurements of Jiménez et al. (2010a).

Appended Hull DARPA SUBOFF

Wall-resolved LES of the appended hull SUBOFF is performed at $Re = 1.2 \times 10^6$, based on the hull length. Figure 10 shows a contour of instantaneous x -velocity in the x - y plane. The addition of the sail and stern appendages significantly complicates the flow-field. Each appendage generates a junction vortex at its base as well as a pair of counter-rotating vortices at its tip, which originate from the pressure gradient between the tip of the appendage and its curved sides. The junction vortex in the wake of the sail transports high momentum fluid closer to the hull surface, locally reducing the boundary layer thickness compared to the lower side of the hull. This effect is visible in the near wake of the sail in Figure 10.

Figure 12 shows the pressure coefficient on the upper meridian of the hull and appendages ($z = 0$ and $y > 0$) compared to experimental measurements of Huang et al. (1992) at $Re = 1.2 \times 10^7$. The experimental measurements have been corrected for blockage effects, as detailed in Huang et al. (1992). In addition, Figure 13 compares the pressure coefficient on the sail at 10% of the sail height to the same experimental data set. Both comparisons show good agreement with the experiments, despite the difference in Reynolds number.

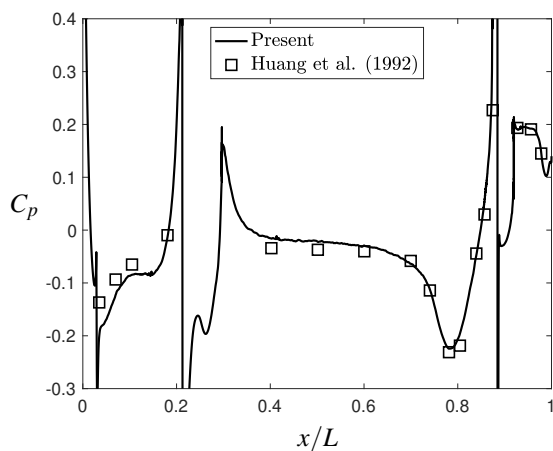


Figure 12: Flow over the appended hull: pressure coefficient on the upper meridian of the hull and appendages ($z = 0$, $y > 0$) compared to the experimental measurements of Huang et al. (1992) at $Re = 1.2 \times 10^7$.

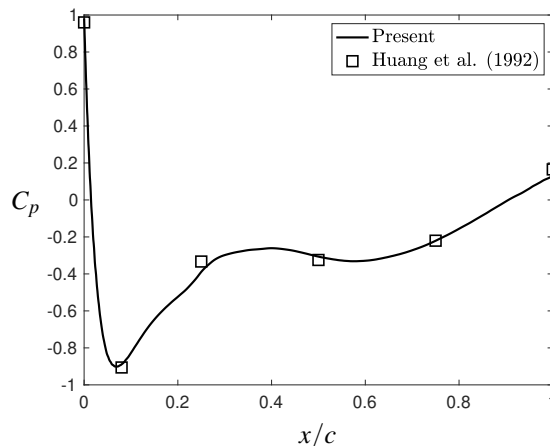


Figure 13: Flow over the appended hull: pressure coefficient on the sail at 10% of the sail height compared to the experimental measurements of Huang et al. (1992) at $Re = 1.2 \times 10^7$.

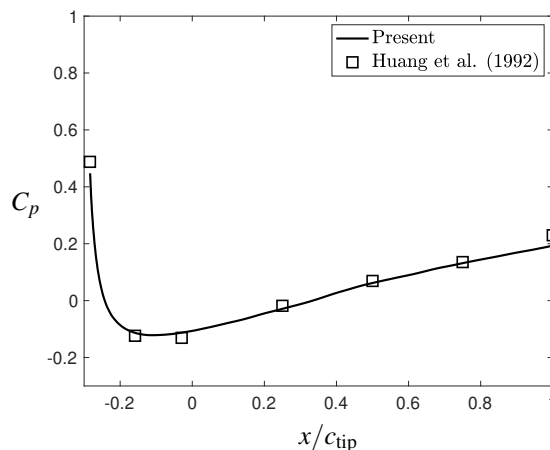


Figure 14: Flow over the appended hull: pressure coefficient on the upper stern appendage at 10% of the stern appendage height compared to the experimental measurements of Huang et al. (1992) at $Re = 1.2 \times 10^7$.

While the sail encounters a relatively thin boundary layer, the boundary layer approaching the stern appendages is significantly thicker and is evolving under an adverse pressure gradient. The accurate simulation of the hull boundary layer is essential to predict the performance of the stern appendage control surfaces. The curvature of the stern appendages introduces additional pressure gradients to the stern compared to the unappended case, and the resulting junction vortices and wakes produced by each appendage would be ingested by a stern-mounted propeller. Figure 14 shows the pressure coefficient at 10% of the stern appendage height versus

the tip chord of the stern appendage. This area of the stern appendage is completely immersed in the hull boundary layer and as a result the stagnation pressure at the leading edge is much lower than the for the sail. Again, there is good agreement with the measurements of Huang et al. (1992).

Forward Mode for Propeller P4381

For forward mode of operation, the simulation is started at target Re and is run for a total of 25 revolutions. The simulation is performed with a time step of 0.005 unit or 2133.6 computational time steps per propeller rotation. Run times are about 2 seconds a time step. Flow statistics and unsteady loads are collected for the 20 revolutions. The near wake is validated qualitatively and quantitatively. The results are compared to the 36 in. water tunnel experiments (WT) and open water towing-tank experiments (OW) by Jessup et al. (2004, 2006). The main flow features in the propeller wake are the helical tip vortices and the hub vortex, figure 15.

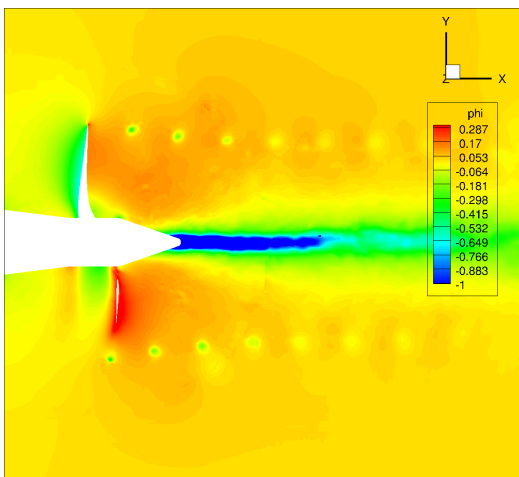


Figure 15: The flow field in forward mode showing pressure. The low pressure regions represent the helical tip vortices. Note the helical tip vortices and the hub vortex being convected downstream the propeller and through the two meshes.

Mean Flow Fields

The time-averaged flow field comparison is focused on the near-wake region in the blade wake. In the blade trailing edge, the thin vortex sheet is capture. Overall, we see good qualitative agreement compared to previous PIV measurements from experiments and simulations, figure 17. A quantitative comparison is done as the results are compared to PIV measurements by extracting profiles of different flow parameters at several locations, figure 16. Overall good agreement is shown here as well.

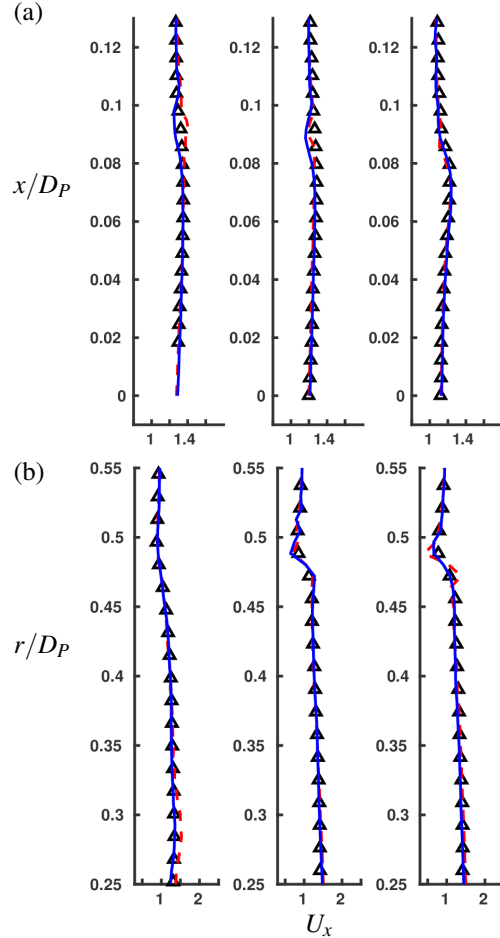


Figure 16: Profiles of U_x at different downstream locations: \triangle is WT experiments (Jessup et al., 2004), $---$ is LES (Kumar and Mahesh, 2017), and $—$ is the present result. The locations from left to right on (a) are $x/D_P=0.06$, $x/D_P=0.08$, $x/D_P=0.10$. The locations from left to right on (b) are $r/D_P=0.35$, $r/D_P=0.40$, $r/D_P=0.45$

	$\langle K_T \rangle$	$\langle K_Q \rangle$
Present	0.20	0.040
LES	0.21	0.041
OW	0.20	0.042
WT	0.18	0.038

Table 4: Mean of the unsteady loads for $J = 0.889$. WT and OW (Jessup et al., 2004, 2006), LES (Kumar and Mahesh, 2017).

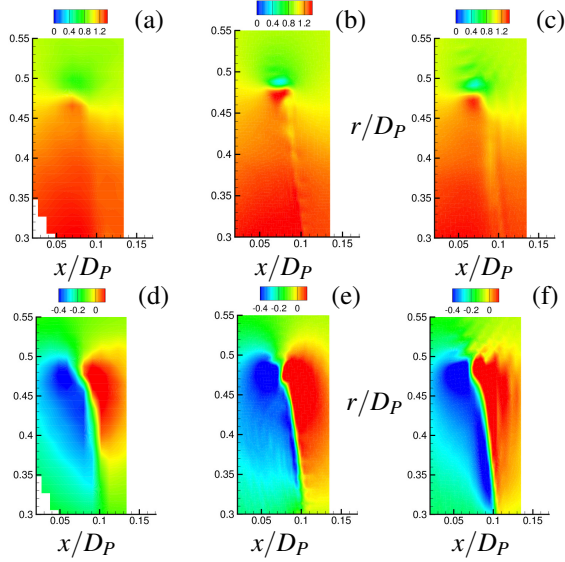


Figure 17: Time-averaged flow contours in the blade wake. (a) and (d) WT experiments (Jessup et al., 2004), (b) and (e) LES (Kumar and Mahesh, 2017), (c) and (f) Present. (a), (b), and (c) show U_x . (d), (e), and (f) show U_r . The resolution on the present result is higher than the experiments but lower than that of the LES comparison.

Propeller Loads

To compare statistics, The mean K_T and K_Q both match well compared to both experiments and previous simulations table 4. Differences between the WT and OW results are attributed to tunnel effects in the water tunnel experiments. These results match well with the previous LES by Kumar and Mahesh (2017), though on a coarser grid.

Crashback for Propeller P4381

For crashback, a solution is interpolated from a previous solution, in order to avoid initial transients from the initial condition. The simulation is ran for over 300 revolutions with a time step of 0.004 unit or 2100 computational time steps per propeller rotation. Run times are about 1.5 seconds a time step.

The instantaneous flow field shows the unsteady ring vortex caused by the interaction of the free-stream and propeller induced reverse flow. Note that the ring vortex is asymmetric and unsteady moving between the background and propeller meshes, figure18.

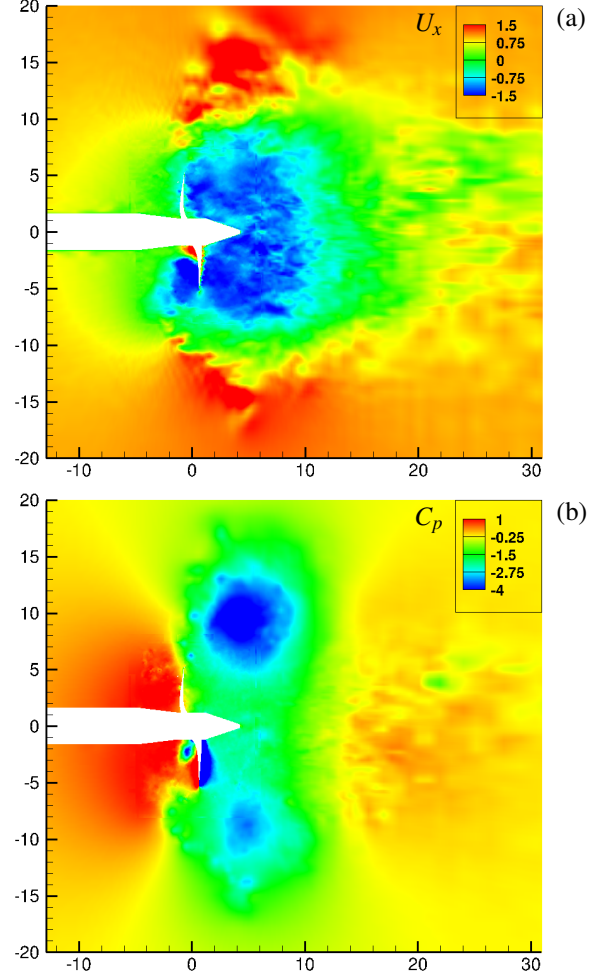


Figure 18: A slice showing the instantaneous flow field and the the ring vortex that is between the two overlapping meshes.

Mean Flow Fields

The time-averaged flow field data is circumferentially averaged and compared to LDV measurements by Jessup et al. (2004) in the X-R plane and previous simulations by Jang and Mahesh (2013). Contours for axial velocity U_x and resolved turbulent kinetic energy k are shown on figure 20. Overall circumferential average fields and the mean location of the ring vortex core show good agreement, figure 21. For a quantitative comparison, profiles are extracted at different x locations in the near propeller field and compared to the experiments and previous simulations showing good agreement, figure 19.

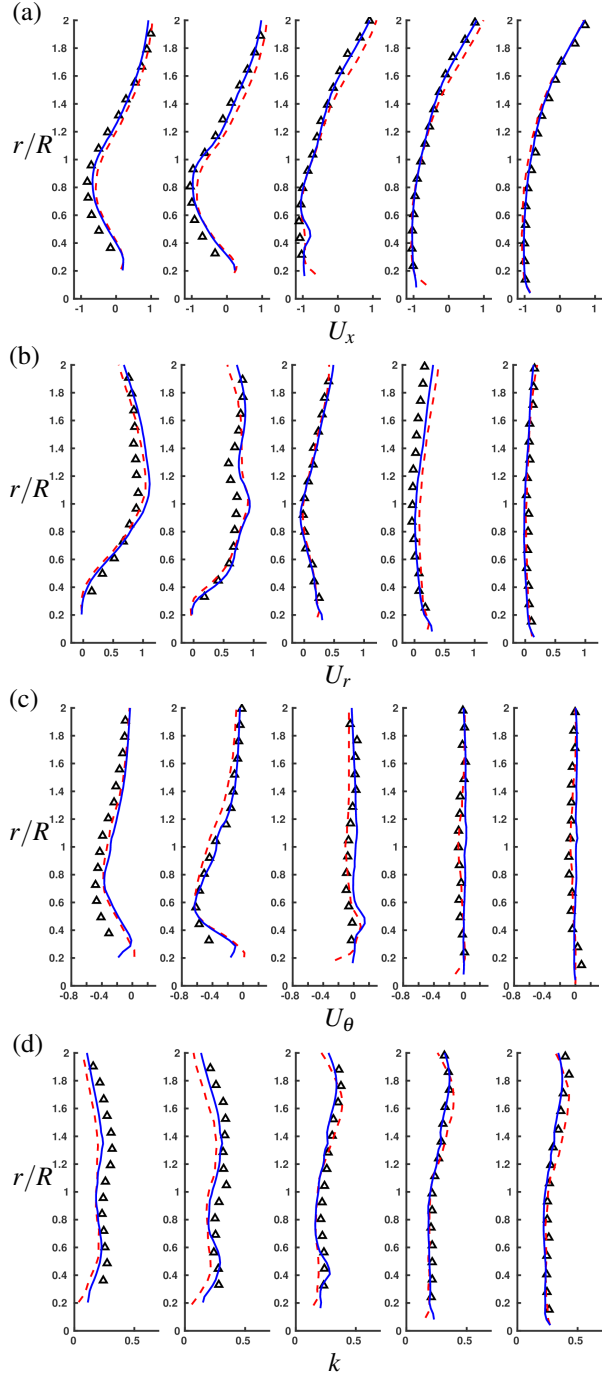


Figure 19: Profiles of U_x , U_r , U_θ , and k at different downstream locations: \triangle is WT experiments (Jessup et al., 2004), $---$ is LES (Jang and Mahesh, 2013), and $—$ is the present result. The locations are from left to right $x/R=-0.39$, $x/R=-0.25$, $x/R=0.25$, $x/R=0.75$, where R is the propeller radius.

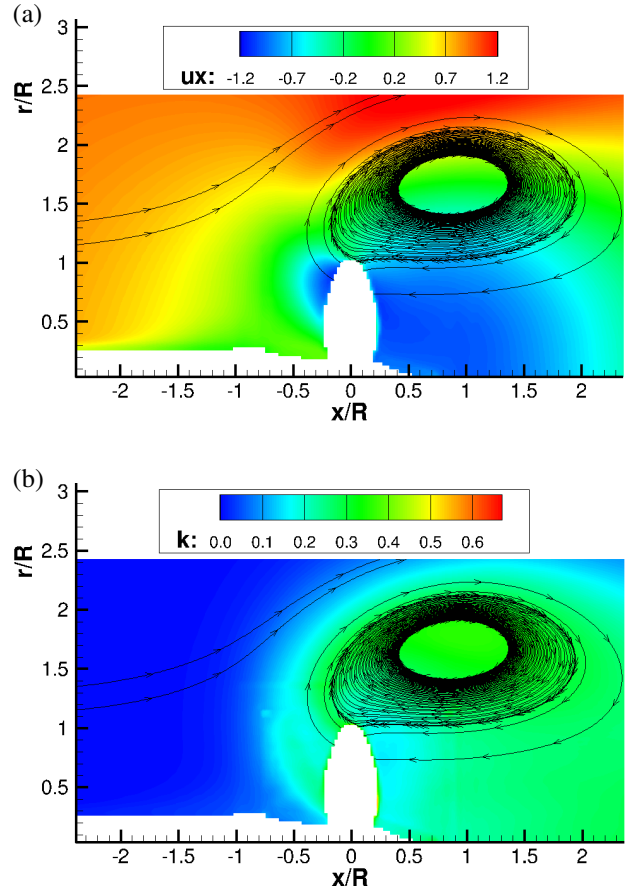


Figure 20: Circumferentially averaged flow fields showing (a) axial velocity U_x and (b) resolved turbulent kinetic energy k with streamlines. Note that the highest levels of k are in the vortex ring core.

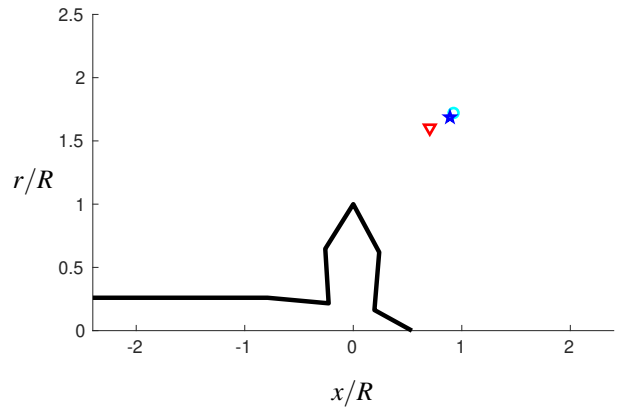


Figure 21: Mean vortex location compared to previous experiments and publications. \circ is WT experiments (Jessup et al., 2004), ∇ is LES (Jang and Mahesh, 2013), and \star is the present result.

Propeller Loads

Crashback is known for the unsteadiness of the ring vortex which has a major effect on the propeller loads. Time history is shown on 22. Propeller load statistics are compared to previous experiments and computations showing good agreement on table 5. K_T and K_Q compare well to previous LES (Jang and Mahesh, 2013) and are between the WT and OW results. Standard deviations match well with the fine grid simulation by (Jang and Mahesh, 2013). The side force coefficient K_S results compare well throughout.

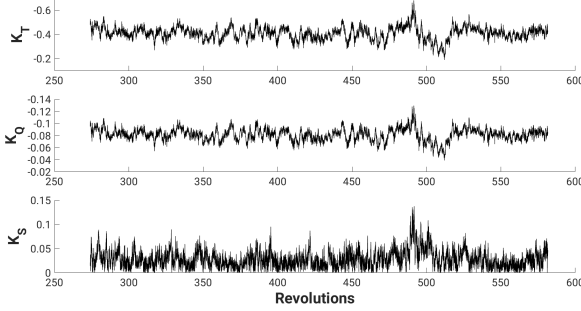


Figure 22: Unsteady load history for the force coefficients. Note the unsteadiness and low frequency high amplitude events.

	$\langle K_T \rangle$	$\sigma(K_T)$	$\langle K_Q \rangle$	$\sigma(K_Q)$	$\langle K_S \rangle$
Present	-0.41	0.053	-0.081	0.010	0.029
LES (Coarse)	-0.39	0.062	-0.078	0.012	0.035
LES (Fine)	-0.38	0.055	-0.074	0.027	0.027
WT	-0.33	0.060	-0.065	0.011	0.030
OW	-0.41	-	-0.078	-	-

Table 5: Statistics of unsteady loads for $J = -0.7$. LES (Jang and Mahesh, 2013), WT (Jessup et al., 2004) and OW (Jessup et al., 2006)

The Power Spectral Density (PSD) of the force coefficients are compared to experiments and previous LES computations on figure 23. PSD is computed by dividing time histories of unsteady loads into N segments with 50 percent overlap. Each segment is filtered using the Hanning window to minimize end effects, rescaled to maintain the original energy, and transformed into spectral domain using the Fast Fourier Transform (FFT). The PSD computed for each segment are averaged over all segments. There's a peak at the blade passage frequency 5 rev^{-1} and low frequency peaks that can impact maneuverability. Just like for (Jang and Mahesh, 2013) we see the spectra deviate from experiment at frequencies greater than 10 rev^{-1} .

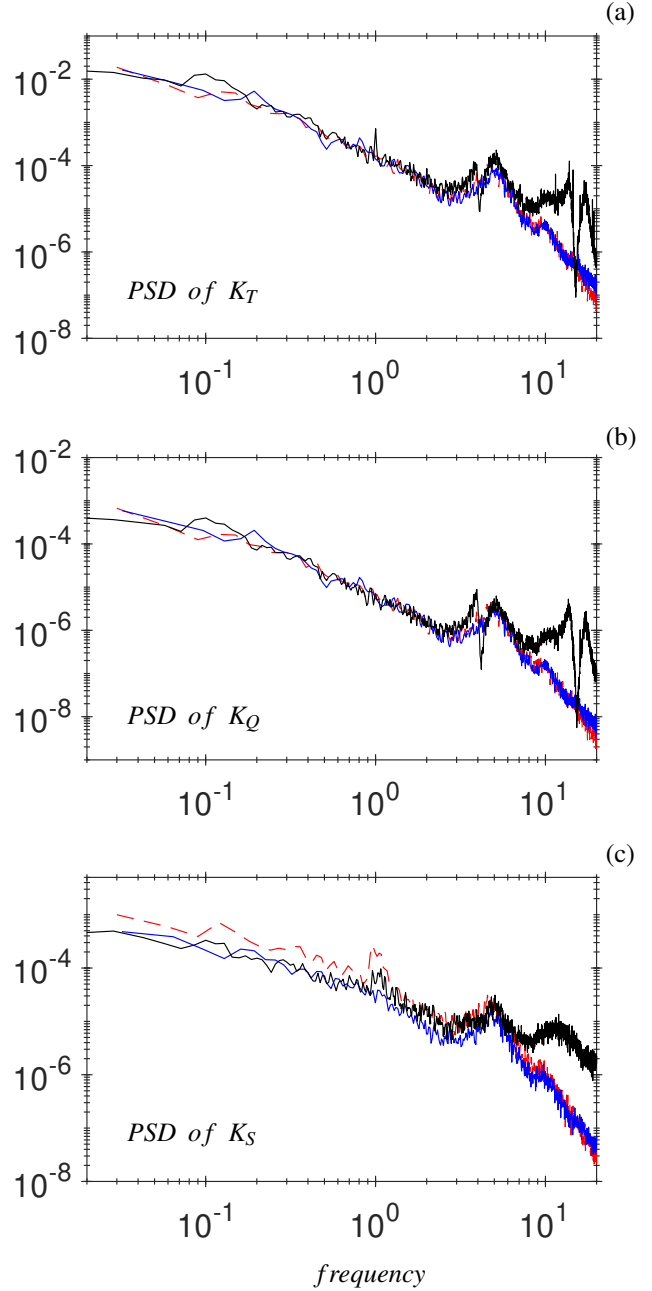


Figure 23: PSD of the force coefficients (a) K_T , (b) K_Q , (c) K_S where — is WT experiments (Jessup et al., 2004), - - - is LES (Jang and Mahesh, 2013), and — is the present result.

SUMMARY AND FUTURE WORK

A novel unstructured overset methodology has been applied to building-block problems with the goal of

simulating maneuvering marine vehicles. For the bare hull and appended hull cases, the use of body-fitted grids helps attain high wall resolution to capture the hull boundary layer and its interaction with sail and appendage flow features while simplifying grid generation. For propeller P4381, rigid body rotation is successfully used to simulate rotation of the propeller while the method's flexibility in grid generation is used. Reasonable run times and computational cost make it possible to capture low frequency events in the unsteady loading for crashback. Comparisons to experiments and other simulations shows good agreement for both cases. Overall, this work brings us a step closer to the goal of LES of maneuvering marine vehicles. Future simulations will focus on assembling these building block problems to simulate self-propulsion and other maneuvers. Essential to these future simulations are experimental measurements of hull forms that include both wake and boundary layer measurements and flow-field measurements of propelled configurations.

ACKNOWLEDGEMENT

This work was supported by the United States Office of Naval Research (ONR) under ONR Grant N00014-18-1-2356 with Dr. Ki-Han Kim as grant monitor. Computational resources were provided by the U.S. Army Engineer Research and Development Center (ERDC) in Vicksburg, Mississippi on the Cray XE6, Copper of High Performance Computing Modernization Program (HPCMP) and the Minnesota Supercomputing Institute (MSI) at the University of Minnesota. The authors thank S. Anantharamu for his assistance with pre-processing of the grids for the massively parallel computations reported in this work and Dr. Praveen Kumar for his assistance and input in grid generation.

REFERENCES

- Alin, N., Bensow, R. E., Fureby, C., Huuva, T., and Svennberg, U. "Current capabilities of DES and LES for submarines at straight course". Journal of Ship Research, 54(3):184–196, 2010.
- Bensow, R. E., Fureby, C., Liefvendahl, M., and Persson, T. "A comparative study of rans, des and les". In 26th Symposium on Naval Hydrodynamics, Rome, Italy, 2006.
- Bridges, D. H. "A detailed study of the flowfield of a submarine propeller during a crashback maneuver". Technical Report MSSU-ASE-04-1, Department of Aerospace Engineering, Mississippi State University, 2004.
- Chang, P., Ebert, M., Young, Y. L., Liu, Z., Mahesh, K., Jang, H., and Shearer, M. "Propeller forces and structural responses to crashback". In Proceedings of the 27th Symposium on Naval Hydrodynamics, Seoul, Korea, 2008.
- Chase, N., Michael, T., and Carrica, P. M. "Overset simulation of a submarine and propeller in towed, self-propelled and maneuvering conditions". International Shipbuilding Progress, 60(1-4):171–205, 2013.
- Chen, B. and Stern, F. "Computational fluid dynamics of four quadrant marine propeller flow". Journal of Ship Research, 43:4:218, 1999.
- Clauser, F. H. "Turbulent boundary layers in adverse pressure gradients". Journal of the Aeronautical Sciences, 21(2):91–108, 1954.
- Davoudzadeh, F., Taylor, L. K., Zierke, W. C., Dreyer, J. J., McDonald, H., and Whitfield, D. L. "Coupled Navier–Stokes and equations of motion simulation of submarine maneuvers, including crashback". In Proceedings of the 1997 ASME Fluids Engineering Division Summer Meeting, New York, 1997.
- Germano, M., Piomelli, U., Moin, P., and Cabot, W. H. "A dynamic subgrid–scale eddy viscosity model". Physics of Fluids A, 3:7:1760, 1991.
- Groves, N. C., Huang, T. T., and Chang, M. S. Geometric Characteristics of DARPA suboff models:(DTRC Model Nos. 5470 and 5471). David Taylor Research Center, 1989.
- Horne, Wyatt James and Mahesh, Krishnan. "A massively-parallel, unstructured overset method for mesh connectivity". Journal of Computational Physics, 376:585–596, 2019a.
- Horne, Wyatt James and Mahesh, Krishnan. "A massively-parallel, unstructured overset method to simulate moving bodies in turbulent flows". Journal of Computational Physics, 397:108790, 2019b.
- Huang, T., Liu, H. L., Groves, N., Forlini, T., Blanton, J., and Gowing, S. "Measurements of flows over an axisymmetric body with various appendages in a wind tunnel: the DARPA SUBOFF experimental program". In Proceedings of the 19th Symposium on Naval Hydrodynamics, 1992.
- Jang, H. and Mahesh, K. "Large eddy simulation of flow around a reverse rotating propeller". Journal of Fluid Mechanics, 729:151–179, 2013.
- Jessup, S., Chesnakas, C., Fry, D., Donnelly, M., Black, S., and Park, J. "Propeller performance at extreme

- off design conditions”. In Proceedings of the 25th Symposium on Naval Hydrodynamics, St. John’s, Canada, 2004.
- Jessup, S., Fry, D., and Donnelly, M. “Unsteady propeller performance in crashback conditions with and without duct”. In Proceedings of the 26th Symposium on Naval Hydrodynamics, Rome, Italy, 2006.
- Jiang, C. W., Dong, R. R., Lui, H. L., and Chang, M. S. “24-inch water tunnel flow field measurements during propeller crashback”. In Proceedings of the 21st Symposium on Naval Hydrodynamics. The National Academies Press, Washington DC, 1997.
- Jiménez, J., Hoyas, S., Simens, M. P., and Mizuno, Y. “The intermediate wake of a body of revolution at high reynolds numbers”. Journal of Fluid Mechanics, 659: 516–539, 2010a.
- Jiménez, J. M., Reynolds, R. T., and Smits, A. J. “The effects of fins on the intermediate wake of a submarine model”. Journal of Fluids Engineering, 132(3):031102, 2010b.
- Kim, S.-E., Rhee, B. J., and Miller, R. W. “Anatomy of turbulent flow around DARPA SUBOFF body in a turning maneuver using high-fidelity RANS computations”. International Shipbuilding Progress, 60 (1):207–231, 2013.
- Kumar, P. and Mahesh, K. “Large eddy simulation of propeller wake instabilities”. Journal of Fluid Mechanics, 814:361–396, 2017.
- Kumar, P. and Mahesh, K. “Analysis of axisymmetric boundary layers”. Journal of Fluid Mechanics, 849: 927–941, 2018a.
- Kumar, P. and Mahesh, K. “Large-eddy simulation of flow over an axisymmetric body of revolution”. Journal of Fluid Mechanics, 853:537–563, 2018b.
- Lilly, D. K. “A proposed modification of the Germano subgrid-scale closure model”. Physics of Fluids A, 4:3: 633, 1992.
- Mahesh, K., Constantinescu, G., and Moin, P. “A numerical method for large-eddy simulation in complex geometries”. Journal of Computational Physics, 197:1:215, 2004.
- Mahesh, K., Kumar, P., Gnanaskandan, A., and Nitzkorski, Z. “LES applied to ship research”. Journal of Ship Research, 59(4):238–245, 2015.
- Moin, P. and Mahesh, K. “Direct numerical simulation: a tool in turbulence research”. Annual Review of Fluid Mechanics, 30(1):539–578, 1998.
- Park, N. and Mahesh, K. “Reduction of the Germano-identity error in the dynamic Smagorinsky model”. Physics of Fluids (1994-present), 21(6): 065106, 2009.
- Posa, A. and Balaras, E. “A numerical investigation of the wake of an axisymmetric body with appendages”. Journal of Fluid Mechanics, 792:470–498, 2016.
- Posa, A. and Balaras, E. “Large-eddy simulations of a notional submarine in towed and self-propelled configurations”. Computers & Fluids, 165:116–126, 2018.
- Posa, A. and Balaras, E. “A numerical investigation about the effects of reynolds number on the flow around an appended axisymmetric body of revolution”. Journal of Fluid Mechanics, 884, 2020.
- Rotta, J. “On the theory of the turbulent boundary layer”. NACA Technical Memorandum, No. 1344, 1953.
- Schlichting, H. Boundary-layer theory. McGraw-Hill, 1968.
- Verma, A. and Mahesh, K. “A Lagrangian subgrid-scale model with dynamic estimation of Lagrangian time scale for large eddy simulation of complex flows”. Physics of Fluids (1994-present), 24(8):085101, 2012.
- Verma, A., Jang, H., and Mahesh, K. “The effect of an upstream hull on a propeller in reverse rotation”. Journal of Fluid Mechanics, 704:61–88, 2012.
- Vyšohlid, M. and Mahesh, K. “Large eddy simulation of crashback in marine propellers”. In Proceedings of the 26th Symposium on Naval Hydrodynamics, Rome, Italy, 2006.
- Yang, C. and Löhrner, R. “Prediction of flows over an axisymmetric body with appendages”. In The 8th International Conference on Numerical Ship Hydrodynamics, Busan, Korea, 2003.